energies

MDPI

Article

An Anti-Disturbance Extended State Observer-Based Control of a PMa-SynRM for Fast Dynamic Response

Dongyang Li [1], Shuo Wang [1,*], Chunyang Gu [2], Yuli Bao [1], Xiaochen Zhang [2], Chris Gerada [3] and He Zhang [2]

[1] Key Laboratory of More Electric Aircraft Technology of Zhejiang Province, University of Nottingham Ningbo China, Ningbo 315100, China; dongyang.li@nottingham.edu.cn (D.L.); yuli.bao2@nottingham.edu.cn (Y.B.)
[2] Advanced Electrical Machine Drive Research Center, Yongjiang Laboratory, Ningbo 315202, China; chunyang.gu@nottingham.edu.cn (C.G.); xiaochen.zhang@nottingham.edu.cn (X.Z.); he.zhang@nottingham.edu.cn (H.Z.)
[3] Faculty of Engineering, University of Nottingham, Nottingham NG7 2RD, UK; chris.gerada@nottingham.ac.uk
* Correspondence: shuo.wang@nottingham.edu.cn

Abstract: The control system of PMa-SynRMs (Permanent Magnet-assisted Synchronous Reluctance Machines) exhibit susceptibility to external disturbances, thereby emphasizing the utmost significance of employing an observer to effectively observe and suppress system disturbances. Meanwhile, disturbances in load are sensitive to control system noise, which may be introduced from current sensors, hardware circuit board systems, sensor-less control, and analog position sensors. To tackle these problems, this paper proposes an A-DESO (anti-disturbance extended state observer) to improve the dynamic performance, noise suppression, and robustness of PMa-SynRMs in both the constant torque and FW (flux weakening) regions. With the proposed A-DESO, lumped disturbance in torque could be detected, and speed could be extracted in position with unmeasurable noise. Thanks to the merits of the small observation error in the low-frequency region and the excellent anti-disturbance performance in the high-frequency region of the proposed A-DESO, the control of the PMa-SynRM features the advantages of a fast response and good noise immunity ability within the same observation error range. The proposed A-DESO presents a shorter convergence time and a better noise suppression ability, which leads to a better dynamic response of the PMa-SynRM when encountering an unknown load disturbance compared to the traditional ESO-based control, according to simulations and experiments.

Keywords: permanent magnet-assisted synchronous reluctance machine; anti-disturbance extended state observer; unmeasurable disturbance

Citation: Li, D.; Wang, S.; Gu, C.; Bao, Y.; Zhang, X.; Gerada, C.; Zhang, H. An Anti-Disturbance Extended State Observer-Based Control of a PMa-SynRM for Fast Dynamic Response. *Energies* **2024**, *17*, 4260. https://doi.org/10.3390/en17174260

Academic Editor: Mario Marchesoni

Received: 2 July 2024
Revised: 11 August 2024
Accepted: 19 August 2024
Published: 26 August 2024

1. Introduction

A PMa-SynRM demonstrates strong saliency [1]. Ferrite material is inserted into barriers, which improves the power factor and features a higher temperature resistance ability, compared with PMSMs. Compared to induction machines, they exhibit higher efficiency, which will reduce carbon emissions and protect the environment [2]. Despite its advantages, a PMa-SynRM has some shortcomings. Its flux is largely derived from stator current excitation, which results in a low power factor compared to PMSMs [3]. In the high-speed FW region, a PMa-SynRM exhibits strong nonlinear characteristics with inductance, cross-saturation, and self-saturation. As a result, a PMa-SynRM is susceptible to poor torque control accuracy, slow response time, noise, and oscillating repetitively between FW regions and constant torque regions [4].

In actual control systems, the accuracy of the current sensor, position sensor, and the hardware's noise suppression ability are limiting factors. These limitations lead to significant high-frequency noise in the measured current. Furthermore, speed is primarily derived from the sensor-less control or direct differential of position, which is obtained

through analog position sensors [5]. In a typical digital control system, noise can be amplified by post-processing circuits and/or differential conditional links, leading to numerous spikes in the speed signals [6]. The ESO (extended state observer) is a solution that has been proposed to address this issue. The ESO, with its series integral structure [7], can significantly suppress noise, particularly that which arises from the speed calculation process. This suppression capability can, to a certain extent, enhance the dynamic performance and disturbance suppression capabilities of PMa-SynRMs [8]. However, the ESO solution is not without its shortcomings. For instance, excessive disturbance can impact the accuracy of the observation results, a factor that was not considered in [8]. Additionally, in the ESO, inductance data are obtained through the current LUTs (Looking-up Tables). Inaccuracies in current measurement can exacerbate the inductance parameter error, further compounding the error in ESO observation [9]. In this way, the PMa-SynRMs are more sensitive to current noise compared to PMSMs.

In PMa-SynRM control, the response time, the observation error, and the ability to suppress the noise of the current sensor and the position sensor are equally important. The torque and speed observation error will affect the accuracy and stability of control, especially when working near the cross point between the FW operating point and the constant torque operating point. Affected by the speed spike, the controller may repeatedly be bound between the FW region and the constant torque region, which deteriorates the control performance of the controller [4,10]. Although the solution proposed in [10] solves the stability problem of the system to a certain extent, it does not fundamentally alleviate the problem of speed fluctuation. For traditional ESO controllers, the control accuracy, response time, and anti-disturbance ability cannot be obtained at the same time [11]. A better response performance will inevitably sacrifice the anti-disturbance ability of the system. In this way, the ESO should be improved to obtain a better dynamic response.

The extended state observer (ESO) was initially introduced by Han [12,13] for the purpose of estimating unknown velocity and mitigating various disturbances. To further enhance the convergence rate of the observer, the development of the non-linear Extended State Observer (NESO) [12,14] has been undertaken. Recently, a novel NESO grounded in fractional power functions has been proposed in [4] to estimate states within a non-linear system characterized by significant uncertainties, particularly in the lower triangular part of the system matrix. Moreover, several studies have addressed the transient behavior and the "peaking value problem" that arises due to high observer gains [15–17]. In the context of [18], a non-linear bandwidth (NLB) will be designed for the Linear Extended State Observer (LESO) [19] to effectively address this issue.

To further enhance anti-disturbance capabilities, a common approach is the bandwidth parametrization technique [13]. However, as this parametrization cannot increase the overall dynamics of the system, the main goal of the research focuses on the optimized selection of parameters according to the working condition. Another approach to address the trade-off between various factors is to modify the observer design. This problem constitutes an active area of research, with numerous solutions proposed in the existing literature. These solutions could be divided into cascading observers [14,15,19], non-linear gains [16,20], adaptive techniques [17,18], redesigning the local behavior through the combination of different observers [21,22], and low-power structures [23,24]. These improved ESOs proposed complicated structures which are hard to implement in low-cost solutions. An interesting alternative to the methods mentioned above is the integration of an ESO with a KF (Kalman Filter), which is widely recognized as the standard solution for observation and filtration in numerous practical applications [25,26]. In this design, the gains in the ESO are optimized through a standard extended KF design [27,28]. However, the dynamic response and noise suppression ability cannot be guaranteed at the same time. The previous research only focused on the estimation error of the extended state but did not analyze the inner error of the state, which is also of great importance in the speed control of the system. The authors of [5] proposed an improved ESO to observe the disturbance in torque and filter out the noise in speed to obtain a better performance.

However, the improved ESO contains a differentiated link, which may bring unstable factors to the control system.

To further address the mentioned problems in constant torque and the FW control for the PMa-SynRM, a novel A-DESO control method based on a LUT is proposed to solve these problems. The main contributions are as follows:

(a) A new constant toque and FW control strategy based on an A-DESO and a LUT is proposed, which features a small steady-state error, quick response, high anti-load-disturbance, and other lumped disturbance resistant abilities.
(b) Compared with the traditional ESO, the proposed A-DESO features a higher low-frequency amplification gain and a high-frequency noise suppression ability for the disturbance in torque and speed observation under the same error acceptance range.
(c) The oscillation problem caused by speed observation error and amplified noise could be alleviated by adopting the proposed A-DESO.
(d) The A-DESO parameters calculation method was given for PMa-SynRMs, considering stability requirements and parameter mismatch analysis.

The first section of this paper introduces the PMa-SynRM and its control schemes. Section 2 introduces the PMa-SynRM modeling method, Maximum Torque per Ampere (MTPA), and FW control, and builds the ESO model. Section 3 proposes the improved A-DESO model, proves the superiority of the A-DESO, and proposes the calculation method of parameters and proof of stability. The simulation and experiments are carried out in Section 4, which proves that the A-DESO features a fast response at low frequencies and a strong anti-disturbance ability at high frequencies under the same error acceptable range.

2. Methodology of PMa-SynRM Base Speed and Flux Weakening Control

2.1. PMa-SynRM Modeling

The equation for the mechanical model is given in (1) [29],

$$J\frac{\mathrm{d}\omega_\mathrm{m}}{\mathrm{d}t} = T_\mathrm{e} - T_\mathrm{L} - B\omega_\mathrm{m} \tag{1}$$

where J is the moment inertia of the motor; d is a differential operator; ω_m is the mechanical speed in rad/s; T_e is the electrical torque; T_L is the load torque; and B is the coefficient of viscous friction.

As shown in (2), the electrical equation in the d- and q-axis is adopted [29],

$$\begin{cases} u_d = R_s i_d + \frac{d\psi_d}{dt} - \omega_e \psi_q \\ u_q = R_s i_q + \frac{d\psi_q}{dt} + \omega_e \psi_d \end{cases} \tag{2}$$

where u_d and u_q are the voltage of the d- and q-axis, respectively; R_s is the stator resistance; i_d, and i_q are the d- and q-axis currents, respectively; ψ_d and ψ_q are the d- and q-axis flux linkages, respectively; and ω_e is the electrical speed of the PMa-SynRM.

The modeling of the torque calculation is given in Equation (3) [29],

$$T_\mathrm{e} = \frac{3}{2}p\left(\psi_\mathrm{d} i_\mathrm{q} - \psi_\mathrm{q} i_\mathrm{d}\right) \tag{3}$$

where p is the pole pairs of the machine.

2.2. Design of MTPA and FW Control

By using MTPA, $\mathrm{i_d}$, and $\mathrm{i_q}$, we can solve the following constrained optimization problem, ignoring motor parameter variations as shown in Equation (4),

$$T_\mathrm{e} = p\left[\psi_\mathrm{pm} i_\mathrm{s}\cos\beta + \frac{1}{2}\left(L_\mathrm{d} - L_\mathrm{q}\right) i_\mathrm{s}\sin 2\beta\right] \tag{4}$$

where β is the MTPA angle between $\mathrm{i_q}$ and $\mathrm{i_d}$.

As a result of (4), the *d*- and *q*-axis currents should comply in Equation (5) under the MTPA condition [9].

$$\beta = \arcsin\left(\frac{-\psi_{\mathrm{pm}} + \sqrt{\psi_{\mathrm{pm}}^2 + 8\left(L_{\mathrm{d}} - L_{\mathrm{q}}\right)^2 i_{\mathrm{s}}^2}}{4\left(L_{\mathrm{d}} - L_{\mathrm{q}}\right) i_{\mathrm{s}}}\right) \tag{5}$$

Thus, the voltage constraint equation for the PMa-SynRM can be derived as (6).

$$\left(\psi_{\mathrm{q}}\right)^2 + \left(\psi_{\mathrm{d}}\right)^2 \leq \left(\frac{u_{\mathrm{smax}}}{\omega_{\mathrm{e}}}\right)^2 \tag{6}$$

In this paper, the self-saturation, cross-saturation, magnetic-saturation, and inductance variation of the machine were considered to obtain the MTPA and FW curves. Figure 1 shows the inductance and flux of the PMa-SynRM obtained from the FEA (Finite Element Analysis 2024R2) software. According to the *d*- and *q*-axis inductance data of the machine in (c) and (d), the *d*- and *q*-axis inductance is largely influenced by the *d*- and *q*-axis currents. Accordingly, the *d*-axis inductance decreases as the *d*-axis current increases, while the *q*-axis inductance decreases as the *q*-axis current increases. It should be noted that the *d*-axis inductance is affected by both the *d*-axis current and the *q*-axis current.

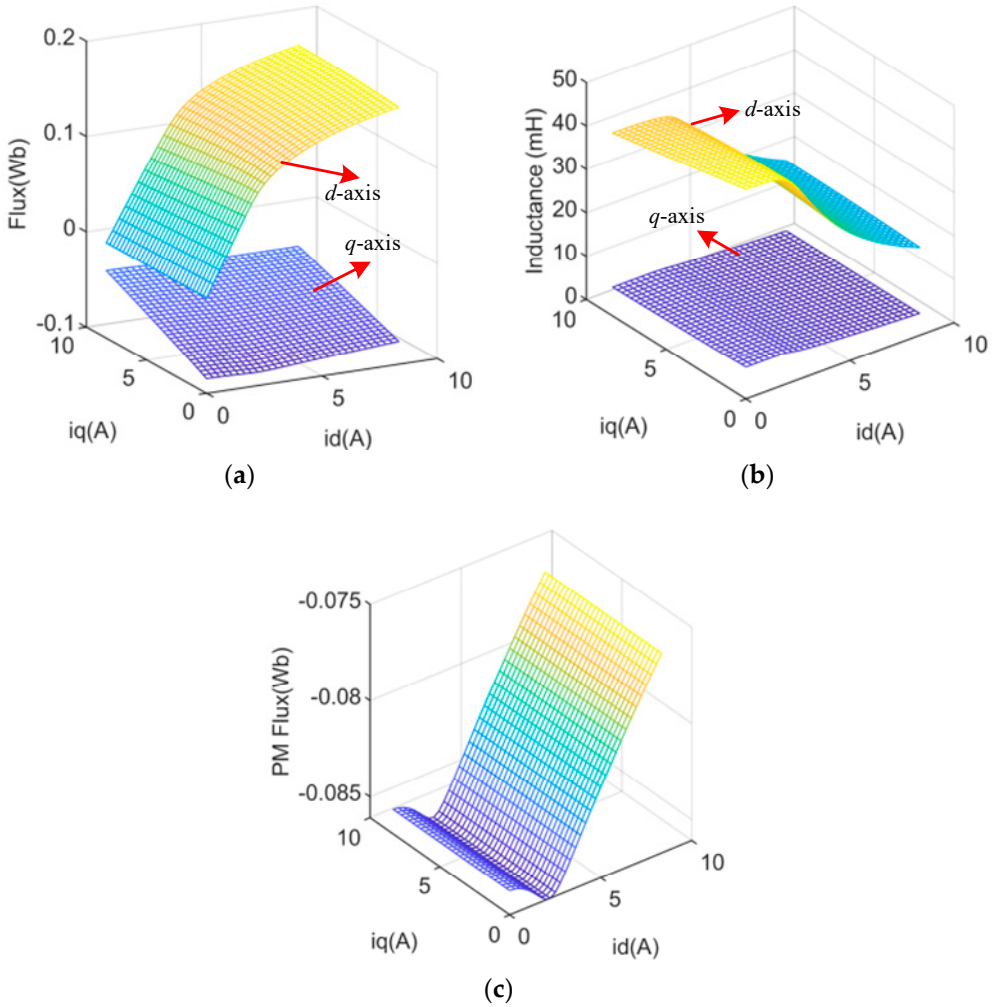

(**a**) (**b**)

(**c**)

Figure 1. Flux characteristics of the PMa-SynRM: (**a**) *d*- and *q*-axis flux with different *d*- and *q*-axis currents; (**b**) *d*- and *q*-axis inductance with different *d*- and *q*-axis currents; and (**c**) permanent magnet flux with different *d*- and *q*-axis currents.

As described in Figure 1, different colors represent the different values of inductance and flux, respectively, in which yellow represents the saturation region. The flux along the *d*- and *q*-axis could also be used for further verification. In (a), as the current increases, the flux linkage gradually decreases and tends to remain unchanged, which means that the magnetic saturation greatly influences the flux and inductance. The change in *q*-axis inductance has the same trend as the change in *d*-axis inductance.

It is possible to calculate the torque of the machine for different currents based on the inductance and flux linkage of the machine as shown in Figure 2. From the calculated maximum torque with the limited current, the MTPA curve with different *d*- and *q*-axis currents could be obtained.

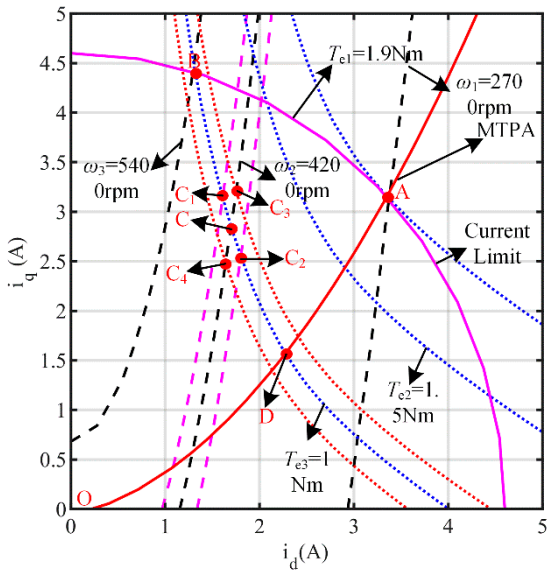

Figure 2. Voltage and current restriction of PMa-SynRM.

The current limitation and voltage limitation curve were shown in Figure 2. The values $\omega 1$, $\omega 2$, $\omega 3$ represent the voltage limitation in different speeds, and $\omega 1 < \omega 2 < \omega 3$. Below the base speed, the current control is maintained on the trajectory of the OA segment, which can ensure minimum copper loss and maximum efficiency. As a result of the cross-saturation, magnetic saturation, and the changes in inductance parameters of the machine shown in Figure 1, the MTPA curve for the OA segment is no longer a straight line. Point A is the rated operating point of the machine. Limited by current and voltage, to obtain a higher speed, the current trajectory needs to move along the AB segments to achieve the higher speeds of $\omega 1$, $\omega 2$, and $\omega 3$. Consequently, it is necessary to reduce the *d*-axis current and increase the *q*-axis current.

Based on the assumption that speed and load torque are known quantities, the working current of the *d*- and *q*-axis currents can be obtained for the working point C. Therefore, a speed calculation method and an ESO are required to get the speed and loaded torque. It was found, however, that there were errors regarding the speed and torque of the load, which are represented by points C1, C2, C3, and C4. In the case of points C1 and C2, if the speed deviates from the desired value (point C), the current trace will move accordingly. Taking C3 and C4 as an example, the control system will adjust its currents to move the working point to C, resulting in a longer settling time for the system. In the case of C1 and C2, the current trace will move along C1 and C2 and even reach D in the constant torque region. This will cause the transient response of the system to deviate from the optimal trajectory, thereby extending the system's settling time. In addition, the system will repeatedly switch between the FW area and the constant torque area, which impairs its stability and dynamic performance. Consequently, the goal is to design an observer that

can reduce torque and speed observation errors while ensuring good dynamic performance and resistance to high-frequency disturbances.

2.3. Design of the Extended State Observer

According to Equations (1) and (3), the speed and electrical angle can be obtained as shown in (7) and (8) [12,13],

$$\dot{\omega}_{\mathrm{m}} = \frac{1}{J}(T_{\mathrm{e}} - B\omega_{\mathrm{m}} - T_{\mathrm{L}}) \tag{7}$$

$$\dot{\theta}_{\mathrm{m}} = \omega_{\mathrm{m}} \tag{8}$$

where θ_{m} is the mechanical angle of the machine.

Using Equations (4) and (7), (9) could be obtained,

$$\dot{\omega}_{\mathrm{m}} = \frac{1}{J}(\frac{3}{2}p(\psi_{\mathrm{d}}i_{\mathrm{q}} - \psi_{\mathrm{q}}i_{\mathrm{d}}) - B\omega_{\mathrm{m}} - T_{\mathrm{L}}) \tag{9}$$

where $B\omega_{\mathrm{m}}$ and T_{L} are the lumped disturbance in torque. The ESO is designed as Equation (10) [8,30],

$$\begin{gathered} \dot{\hat{\omega}}_{\mathrm{m}} = \frac{1}{J}(\frac{3}{2}\mathrm{p}(\psi_{\mathrm{d}}i_{\mathrm{q}} - \psi_{\mathrm{q}}i_{\mathrm{d}}) - d(t) - \beta_1(\hat{\omega}_{\mathrm{m}} - \omega_{\mathrm{m}})) \\ \dot{\hat{T}}_L(t) = -\beta_2(\hat{\omega}_{\mathrm{m}} - \omega_{\mathrm{m}}) \\ \beta_1 = 2\omega_0 \\ \beta_2 = \omega_0^2 \end{gathered} \tag{10}$$

where ˆ represent the observed variables; $\hat{T}_{\mathrm{L}}(t)$ represents the observed load torque; and ω_0 is the cut-off frequency. The parameter selection method is also used to choose β_1 and β_2 [12,13].

3. Analysis of the Control System

This section has been divided into subsections with appropriate subheadings. It provides a concise and precise description of the experimental results, their interpretation, and the experimental conclusions that can be drawn.

3.1. Problem Statement and Parameter Calculation of ESO

Equation (11) can be calculated,

$$\ddot{e} = -\beta_1\dot{e} - \beta_2 e - \left(B\dot{\omega}_m + \dot{T}_L\right) \tag{11}$$

where $\dot{e}$ and $\ddot{e}$ are the first differential of error and second differential error of ω_{m}, respectively. Then, the estimated speed error and the estimated mechanical speed can be derived in the frequency domain as Equation (12).

$$\begin{cases} \frac{e(\mathrm{s})}{\omega_{\mathrm{m}}(\mathrm{s})} = \frac{-\mathrm{s}}{\mathrm{s}^2+2\omega_0\mathrm{s}+\omega_0^2} \\ \frac{\hat{\omega}_{\mathrm{m}}(\mathrm{s})}{\omega_{\mathrm{m}}(\mathrm{s})} = \frac{\beta_2}{\mathrm{s}^2+2\omega_0\mathrm{s}+\omega_0^2} \end{cases} \tag{12}$$

By increasing ω_0, the response performance can be improved, but the observer will be more sensitive to noise [12]. In this way, a trade-off should be reached between the rapidity of estimation and noise immunity in practical applications.

When the ESO becomes stable, the estimation of load disturbance can be obtained as follows in Equation (13),

$$d(t) = T_{\mathrm{L}} + T_{\mathrm{F}} \tag{13}$$

where T_F represents the viscous friction of the system.

Since $\dot{d}(t)$ is bounded by h_0, the following inequality holds in the time domain [13] expressed as Equation (14),

$$|e| \leq \frac{h_0}{\omega_0^2} \tag{14}$$

where h_0 is a constant value related to the error bounding.

According to (14), the maximum estimation error of the ESO is proportional to h_0 if the bandwidth ω_0 is fixed. Therefore, the ESO is highly dependent on h_0 for its estimation accuracy. A higher cut-off frequency can reduce the observation error, but it also amplifies noise and is more sensitive to high-frequency noise. Due to this, in practice, it is necessary to adjust the cut-off frequency ω_0 to maintain an acceptable level of error, noise, and response time. Figure 3 shows the relationship between the maximum error and frequency.

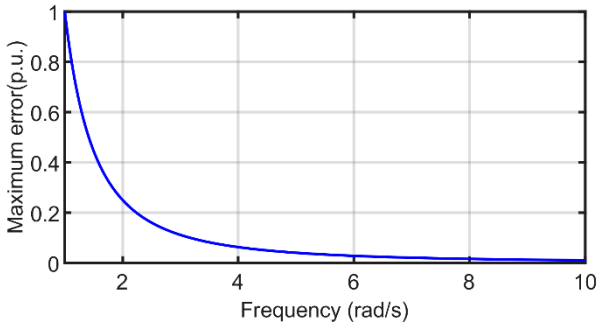

Figure 3. Relationship between maximum error and frequency.

To be more specific, large observed speed errors may result in the control switching repeatedly between the area of FW and the area of MTPA as discussed above, and reducing the control efficiency. However, to obtain a better noise suppression ability, the reduction of the cut-off frequency ω_0 will increase the observation error. As a result, in the control system, noise, observation error, and response time need to be traded off in an effective way.

The purpose of this paper is to design an A-DESO observer to effectively balance the observation error, noise sensitivity, and response time, which features a better response performance in the low frequency and a better noise suppression ability in the high frequency within the same error range simultaneously.

3.2. Traditional ESO Performance

The estimation speed error can be calculated as in Equation (15).

$$\Delta\omega_m(t) = \omega_m(t) - \hat{\omega}_m(t) \tag{15}$$

According to Equation (10), the error dynamic can be obtained as shown in Figure 4. The transfer function from $\dot{T}_L(t)$ to T_L (t) is shown in Equation (16).

$$G_d(s) = \frac{s + 2\omega_0}{s^2 + 2\omega_0 s + \omega_0^2} \tag{16}$$

The ESO has the following properties.

(1) If the total disturbance is a constant one, that is, $\dot{T}_L(t) = 0$,
then the steady error is zero. This means that the ESO could obtain the real value for a constant torque load.

(2) If the load is a ramp one, as in, $\dot{T}_L(t) = C$, the error will converge to $2/\omega_0$. This means that the error existed for a ramp torque load and this error will be decreased with the increase of the cut-off frequency.

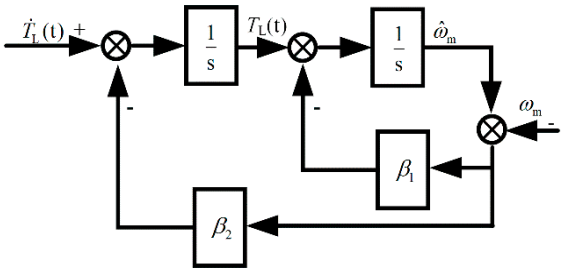

Figure 4. Error dynamics diagram of the ESO.

Figure 5 shows the frequency responses of the disturbance estimation for the ESO. It is shown that the load torque estimation performance improves as ω_0 increases at low frequencies. Therefore, the ESO is effective for slow time-varying disturbances.

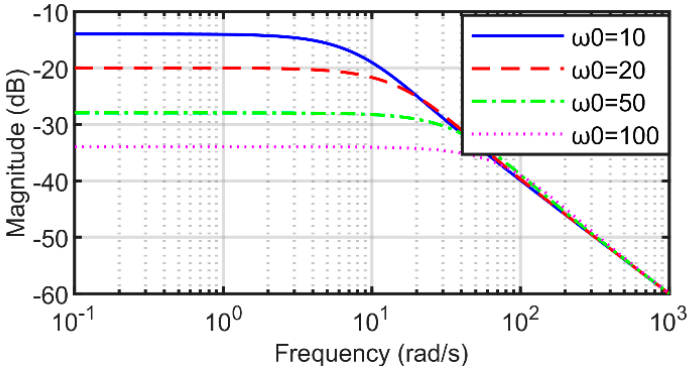

Figure 5. Frequency responses of the ESO error.

In Figure 6, the transfer function from $\omega_m(t)$ to T_L (t) is:

$$G_{\tilde{\zeta}}(s) = \frac{-\omega_0^2 s}{s^2 + 2\omega_0 s + \omega_0^2}. \quad (17)$$

The noise suppression ability and error of the observer need to be balanced. So, the ESO needs to be improved to have a better high-frequency noise suppression capability. In the next subsection, an A-DESO is devised to improve the overall performance and solve the tradeoff.

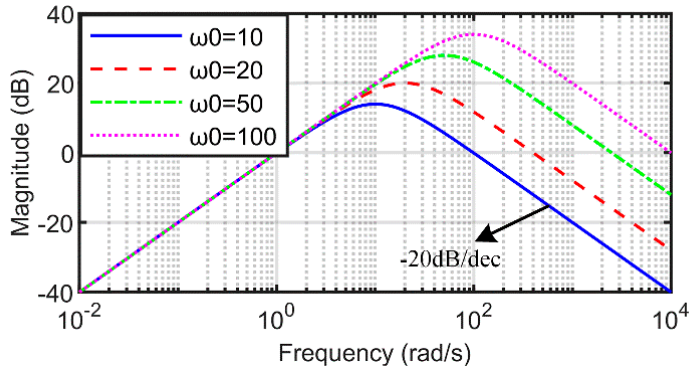

Figure 6. Noise suppression performance.

3.3. Design and Analysis of A-DESO

Since the noise existed in the feedback current, and the calculated speed and the non-linearity of the system are considered as a total disturbance, an A-DESO is proposed

to separate the disturbance estimation from the state reconstruction and it uses a low-pass filter to suppress the unmeasurable noise. The A-DESO is calculated as follows,

$$\begin{cases} \dot{\hat{\omega}}_{\mathrm{m}}(t) = \frac{3}{2}\mathrm{p}(\psi_{\mathrm{d}} i_{\mathrm{q}} - \psi_{\mathrm{q}} i_{\mathrm{d}}) + \beta_1 x_{\mathrm{f}}(t) \\ \dot{\hat{T}}_{\mathrm{L}}(t) = k\beta_1 x_{\mathrm{f}}(t) \\ \dot{x}_{\mathrm{f}}(t) = -\frac{1}{\tau} x_{\mathrm{f}}(t) + \frac{1}{\tau}[\hat{\omega}_{\mathrm{m}}(t) - \omega_{\mathrm{m}}(t)] \\ \hat{y}(t) = \hat{T}_{\mathrm{L}}(t) \end{cases} \tag{18}$$

where $x_{\mathrm{f}}(t)$ is a new state after the filter and r is the time constant.

The error dynamics of the A-DESO is

$$\begin{cases} \dot{\tilde{\omega}}_{\mathrm{m}}(t) = T_{\mathrm{L}}(t) - \beta_1 x_{\mathrm{f}}(t) \\ \dot{\tilde{T}}_{\mathrm{L}}(t) = \dot{T}_{\mathrm{L}}(t) - k\beta_1 x_{\mathrm{f}}(t) \\ \dot{x}_{\mathrm{f}}(t) = -\frac{1}{\tau} x_{\mathrm{f}}(t) + \frac{1}{\tau}[\tilde{\omega}_{\mathrm{m}}(t) - \omega_{\mathrm{m}}(t)] \end{cases} . \tag{19}$$

Figure 7 shows the block diagram of the error dynamics. If $\beta_2 = k\beta_1$ for the ESO and $\tau = 0$ are chosen, then the A-DESO becomes

$$\begin{cases} \dot{\hat{\omega}}_m(t) = u_0(t) + \beta_1[\hat{\omega}_{\mathrm{m}}(t) - \omega_{\mathrm{m}}(t)] \\ \dot{\hat{T}}_{\mathrm{L}}(t) = k\beta_1[\hat{\omega}_{\mathrm{m}}(t) - \omega_{\mathrm{m}}(t)] \\ \hat{y}(t) = \hat{\omega}_{\mathrm{m}}(t) \end{cases} . \tag{20}$$

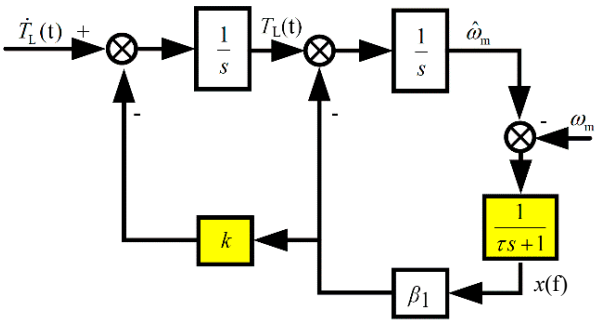

Figure 7. Error dynamics diagram of A-DESO.

According to Figures 4 and 7, Equation (20) yields the traditional ESO. The selection of k is adopted to balance the error and noise suppression performance. The selection of β_1 as the same as the conventional ESO gives

$$\beta_1 = 2\omega_0. \tag{21}$$

3.3.1. Anti-Disturbance Ability for Torque Estimation

The transfer function from $\dot{T}_{\mathrm{L}}(t)$ to $T_{\mathrm{L}}(t)$ is

$$G_d(\mathrm{s}) = \frac{\tau \mathrm{s}^2 + \mathrm{s} + 2\omega_0}{\tau \mathrm{s}^3 + \mathrm{s}^2 + 2\omega_0 \mathrm{s} + 2k\omega_0}. \tag{22}$$

In the proposed A-DESO, $k = 0.75\omega_0$ and $\tau = 0.01$ are selected.

Figure 8 shows that the A-DESO features a better performance than the ESO. In other words, the gain β_1 can be smaller for the A-DESO than for the ESO to achieve the same torque observation error range, which means a better noise suppression ability.

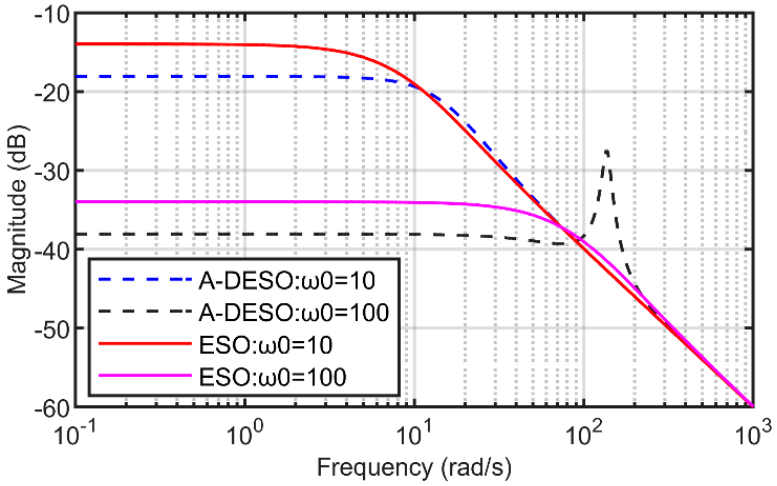

Figure 8. Frequency responses of disturbance estimation error for the A-DESO and ESO.

The transfer function from ω_{m} to $T_{\mathrm{L}}(\mathrm{t})$ in Figure 7 is

$$G_{\tilde{\xi}}(\mathrm{s}) = \frac{-2k\omega_0 \mathrm{s}^2}{\tau \mathrm{s}^3 + \mathrm{s}^2 + 2\omega_0 \mathrm{s} + 2k\omega_0}. \tag{23}$$

Figure 9 shows the frequency responses of the noise suppression ability for the disturbance caused by the speed calculation under the same ω_0. The noise suppression performance is better for the A-DESO than for the ESO at high frequencies when using the same ω_0. On the other hand, to approach the same disturbance estimation performance, ω_0 should be smaller for the ESO than for the A-DESO. In many practical systems, torque inputs are often low frequency and unmeasurable noise signals are often high frequency. The A-DESO provides a way to achieve disturbance rejection and noise attenuation simultaneously.

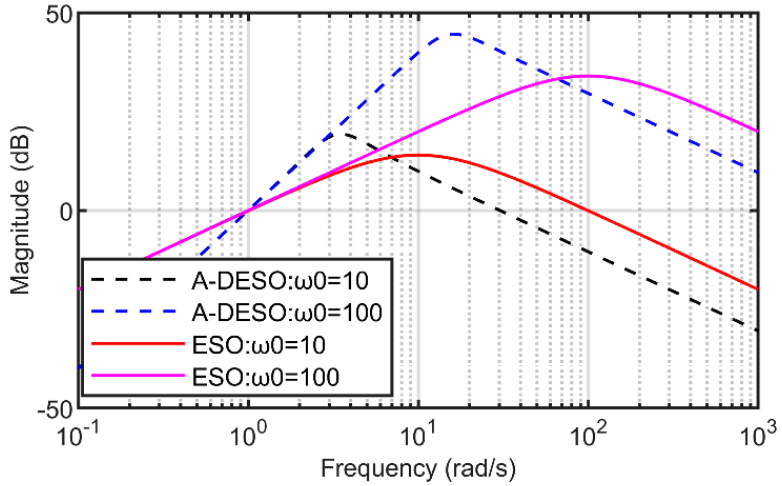

Figure 9. Comparison for noise suppression performance of ESO and A-DESO.

In Figure 9, it can be obtained that the A-DESO features a better error suppression performance than the ESO. For the PMa-SynRM's control system, it achieves a smaller estimate error, a better observer dynamic response, and better noise suppression ability simultaneously using the same ω_0 compared to the conventional ESO.

3.3.2. Anti-Disturbance Ability for Speed Estimation

As discussed above, the speed observation performance will influence the dynamic response of the control system. In this part, the performance of the proposed A-DESO will be analyzed compared to the conventional ESO. The transfer function from $\dot{T}_{\mathrm{L}}(\mathrm{t})$ to $\hat{\omega}_{mest}(t)$ for the conventional ESO can be obtained as Equation (24).

$$G_{\mathrm{L}\omega\mathrm{m}}(\mathrm{s}) = \frac{1}{s^2 + 2\omega_0 s + \omega_0^2} \tag{24}$$

As for the A-DESO, $\dot{T}_{\mathrm{L}}(\mathrm{t})$ to $\hat{\omega}_{mest}(t)$ can be obtained as Equation (25),

$$G_{\mathrm{ADL}\omega\mathrm{m}}(\mathrm{s}) = \frac{\tau\mathrm{s} + 1}{\tau\mathrm{s}^3 + \mathrm{s}^2 + 2\omega_0\mathrm{s} + 2k\omega_0} \tag{25}$$

where k = 0.75 ω_0 and τ = 0.01 are set to investigate the performance of the A-DESO. As can be seen in Figure 9, the error decreases with the increasing of ω_0.

Figure 10 shows that the A-DESO features a better error suppression performance than the ESO does. It means that the speed observation error of the A-DESO is smaller than the conventional ESO when a load disturbance is added. As for the high frequency observation ability, the performance is the same. However, torque disturbance is generally in the low frequency. In this way, the A-DESO features a better speed observation ability in the same ω_0. In other words, the A-DESO features a better noise suppression ability in the same error performance.

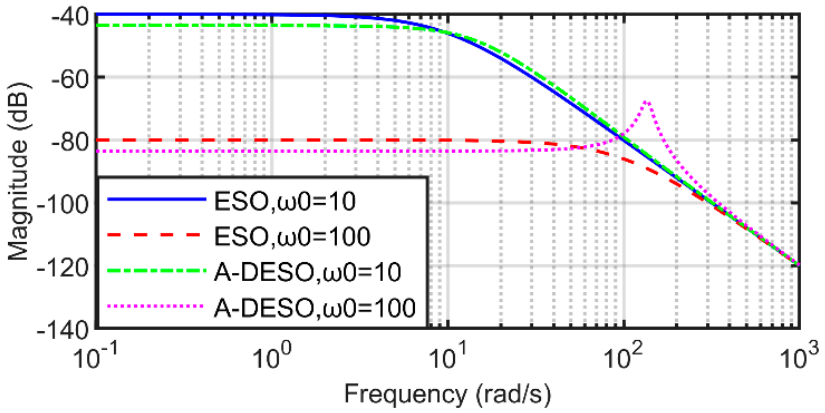

Figure 10. Error dynamic response for speed of ESO and A-DESO.

Then, the noise suppression ability will be analyzed for speed observation. The transfer function from $\omega_m(t)$ to $\hat{\omega}_{mest}(t)$ for the conventional ESO can be obtained as Equation (26).

$$G_{\mathrm{H}\theta}(s) = \frac{-2\omega_0 s - \omega_0^2}{s^2 + 2\omega_0 s + \omega_0^2} \tag{26}$$

As for the A-DESO, the transfer function from $\omega_m(t)$ to $\hat{\omega}_{mest}(t)$ can be obtained as Equation (27).

$$G_{\mathrm{ADH}\theta}(s) = \frac{-2\omega_0 s - 2k\omega_0}{\tau\mathrm{s}^3 + \mathrm{s}^2 + 2\omega_0\mathrm{s} + 2k\omega_0} \tag{27}$$

From Figure 11, to approach the same disturbance estimation performance, ω_0 should be smaller for the ESO than for the A-DESO. For instance, when ω_0 = 100, the magnitude approximates −54 dB and −36 dB at high frequencies. So, the A-DESO features a better noise suppression ability than the ESO. Furthermore, the slope of the IESO is −40 dB/dec, while −20 dB/dec for the ESO, which indicates that the A-DESO features a better noise suppression ability in the high frequency.

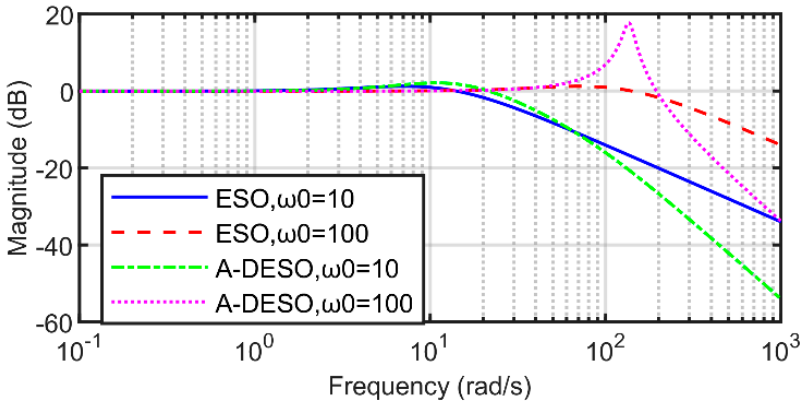

Figure 11. Error suppression response for position observation of ESO and A-DESO.

3.4. Stability of A-DESO and Parameter Design

As described in Section 2, the PMa-SynRM system was regarded as a linear one, in which the non-linearity was not discussed in this paper. To ensure the stability of the system, we need to ensure both the stability of the control system and the stability of the observer. This part discusses the stability of the A-DESO observations under the PMa-SynRM control system.

Figure 12 shows the parameters relationship between the response ability in the low frequency domain. It can be seen that τ has little influence on the low frequency response while k directly determines the response ability of the low frequency. In summary, k needs to be adjusted to determine the low frequency response for the PMa-SynRM.

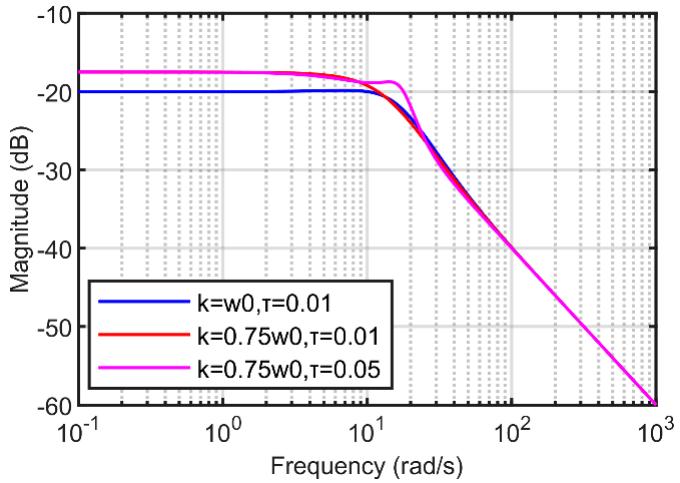

Figure 12. Frequency responses of load torque estimation with different k and τ.

There is an equivalent stability of the A-DESO system. In order to satisfy the stability conditions, Equation (28) should be satisfied.

$$\tau s^3 + s^2 + \beta_1 s + \beta_1 k_1 = 0 \tag{28}$$

From the above equation, the stability criterion can be obtained according to the Routh–Hurwitz stability criterion,

$$\tau k < 1 \tag{29}$$

where $\tau > 0$ and $k > 0$ should be satisfied.

As for the parameter design of the A-DESO, the bandwidth of the A-DESO should be larger than the bandwidth of the control system, so that the rapidity and stability can be guaranteed. According to Equation (29), the stability of the A-DESO deteriorates with the

increase of τ, where τ represents the anti-disturbance ability of the control system. In other words, the anti-disturbance ability and the stability of the system should be balanced.

Figure 13 shows the parameters relationship between the noise suppression ability in the high frequency domain. It can be seen that k has little influence on the noise suppression ability while τ directly determines the response of the high frequency domain. In summary, τ needs to be adjusted to determine the high frequency response for the PMa-SynRM.

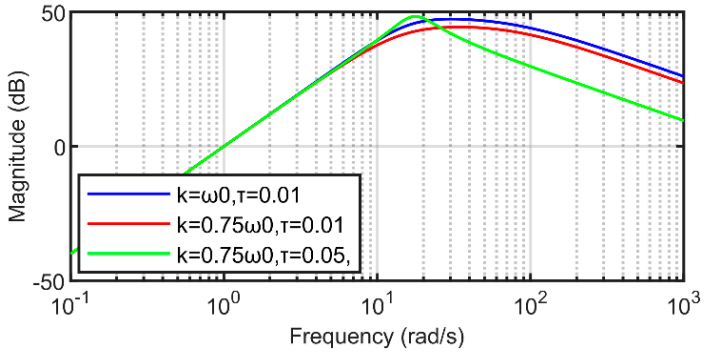

Figure 13. Frequency responses of noise suppression with different k and τ.

In general, the noise from the sensor should be considered; thus, τ can be decided. Then, k can be decided to meet Equation (29). To sum up, the parameter design process of the whole control system can be described as Figure 14.

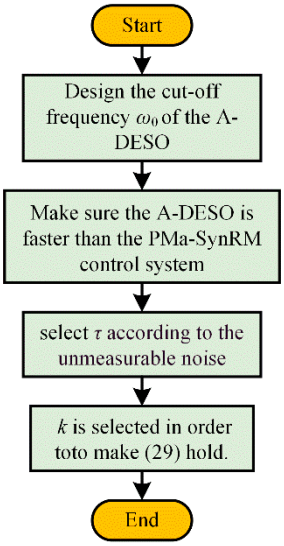

Figure 14. Parameter calculation process of A-DESO based on the PMa-SynRM.

3.5. Parameter Mismatch Analysis

The proposed adaptive ESO requires the knowledge of stator resistance and inductance. As a result of magnetic saturation, the inductance will vary under different load conditions. It is possible to describe the influence of parameter mismatch on the estimated disturbance in the following manner: in Equation (30), the variation of resistance of winding is not considered in this paper.

$$d(t) = \frac{3}{2J}\mathrm{p}((L_\mathrm{d} + \Delta L_\mathrm{d})i_\mathrm{d}i_\mathrm{q} - (L_\mathrm{q} + \Delta L_\mathrm{q})i_\mathrm{q}i_d) + T_\mathrm{L} + T_\mathrm{F} \tag{30}$$

Figure 15a shows the observation error with d- and q-axis inductance mismatch in the rated-load condition. From the calculated data, its observation error of torque is not linear with the inductance mismatch error absolutely. Meanwhile, the observation error of

torque is bounded, which is the most fundamental condition to ensure that the observer can converge in the finite time. Figure 15b shows the observation error with *d*- and *q*-axis inductance mismatch in the half-load condition. The same results can be obtained compared to (a). In Figure 15, the colors represents the value of the observed error.

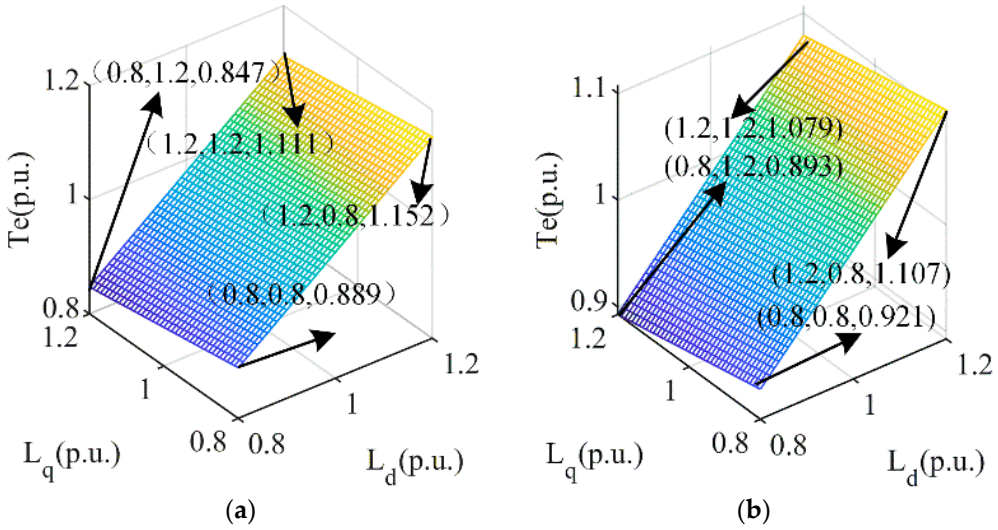

(**a**) (**b**)

Figure 15. Observation error with *d*- and *q*-axis inductance mismatch: (**a**) observation error in rated-load condition; (**b**) observation error in half-load condition.

3.6. Overall Control Diagram

The control diagram of the whole control system is shown in Figure 16. Through the first stage PID controller, the given speed is compared with the observed speed feedback from the A-DESO to determine the torque. Then, the calculated torque is combined with the observed speed and the observed load torque is obtained from the A-DESO to calculate an optimal current. After that, the *d*- and *q*-axis current PI controller is used to get the modulated *d*-and *q*-axis voltage.

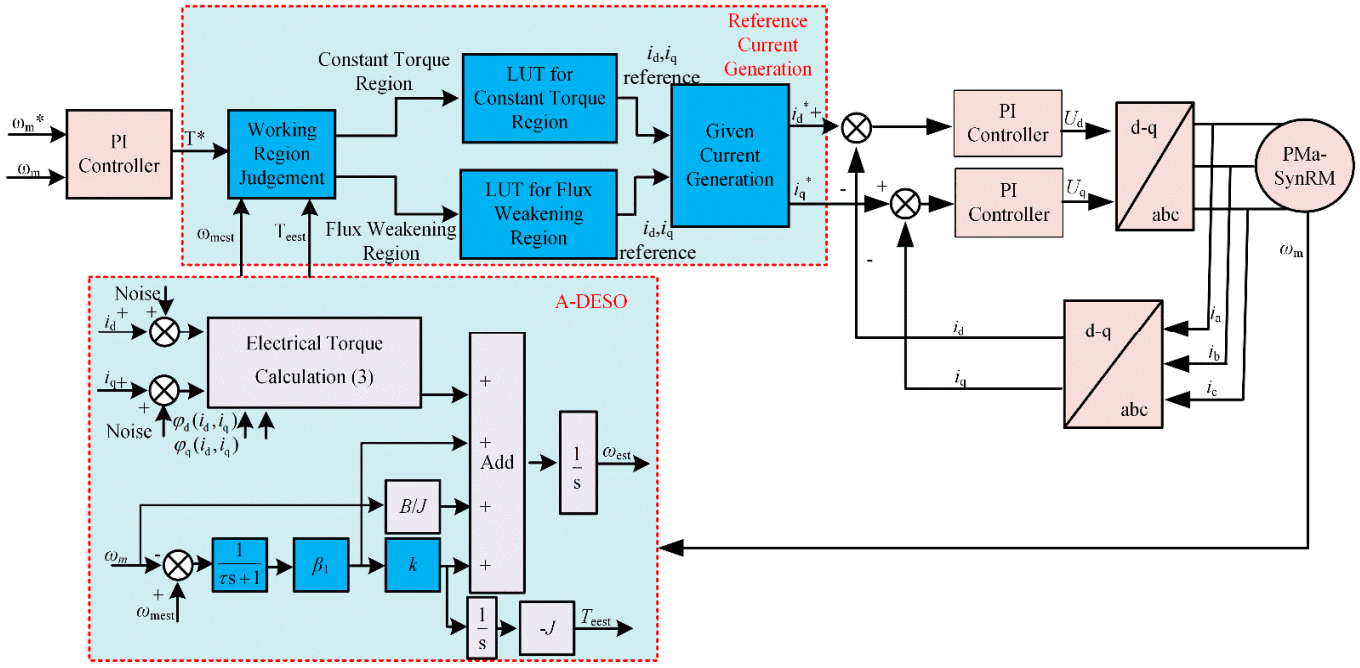

Figure 16. Overall control diagram.

In Figure 17, the MTPA LUT was obtained according to Figure 1 and the FW LUT was derived from Figures 1 and 2 with the input of the lumped disturbance and observed speed.

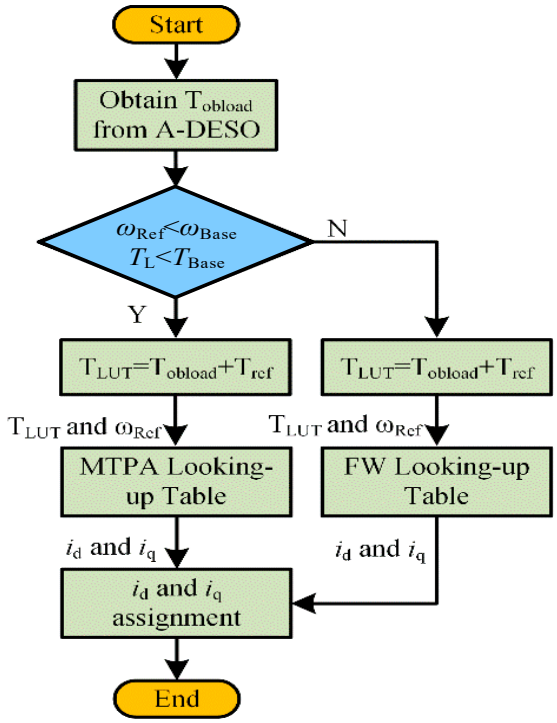

Figure 17. Overall control diagram of i_d and i_q generation.

3.7. Setup of Control Platform

Experimental tests were carried out in this paper in order to verify the feasibility of the algorithm. Figure 18 illustrates the main experimental platform, which mainly consists of the Sugawara test bench for loading and unloading. The YAKOGAWA power analyzer is used for the three-phase voltage and current data acquisition. Meanwhile, oscilloscopes were mainly used to measure voltages and currents. For the converter part of the board, AC power was used, whereas DC power was used for the control part. The STM32F303 microcontroller (STMicroelectronics, Geneva, Switzerland) was used to achieve the proposed algorithm and the maximum peak current of 15 A can be satisfied with the help of the STG series IGBT.

Figure 17 illustrates an algorithm for determining the i_d and i_q components of the current in a control system. The process begins with obtaining the load torque from an A-DESO. The algorithm then checks two conditions: whether the reference speed is less than the base speed and whether the load torque is less than the base torque.

If both conditions are met (Y), the algorithm proceeds to calculate T_{LUT}, which is then used along with speed reference to look up values in the MTPA table to determine the i_d and i_q currents. These currents are then assigned.

If either condition is not met (N), the algorithm calculates T_{LUT} and uses it along with the speed reference to look up values in the FW table. The i_d and i_q currents are then determined from this table and assigned.

To operate the setup in Figure 16, start by powering on the AC and DC supplies, followed by initializing the controller to manage the PMa-SynRM. Activate the Sugawara Test Bench to apply the mechanical load. Monitor the electrical parameters using the power analyzer and observe waveforms on the oscilloscope. Collect and analyze the data via the connected PC, verifying key measurements with the multimeter. Once testing is complete, shut down the system in reverse order, ensuring all data is saved.

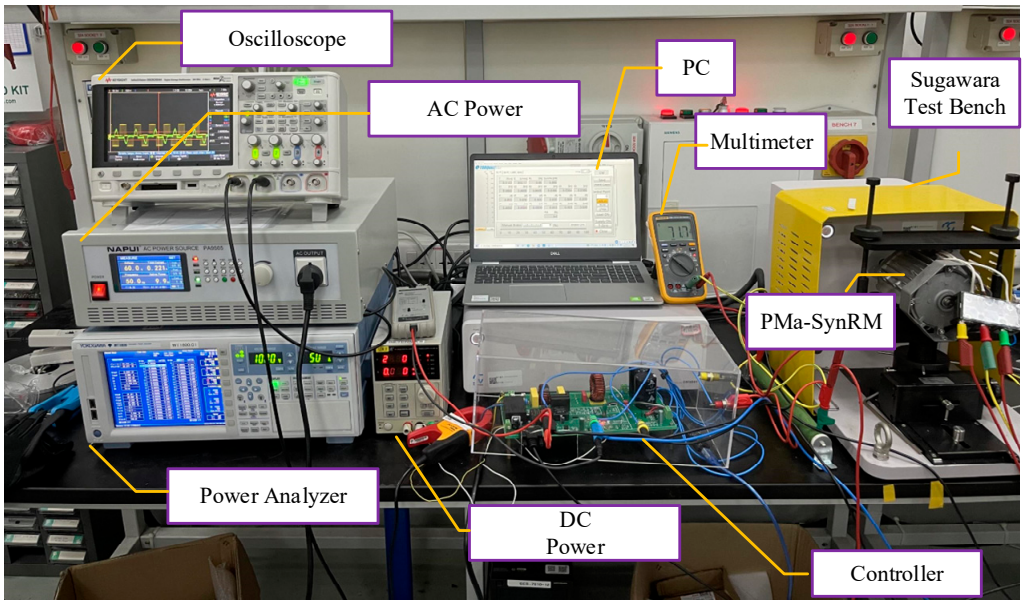

Figure 18. Hardware testbench of PMa-SynRM.

4. Simulations and Experiments

Throughout the entire system, the control part and the drive part were integrated onto a single circuit board based on the STM32F303 platform.

4.1. Simulation Parameters

The parameters of the PMa-SynRM are shown in Table 1.

Table 1. PMa-SynRM Parameters.

Symbol	Definition	Values with Unit
n	rated speed	2700 rpm
T_e	rated torque	1.9 Nm
i_{ab}, i_{bc}, i_{ca}	rated current (RMS)	3.265 A
u_a, u_b, u_c	rated voltage (RMS)	110.0 V
p	pole pairs	2
L_d	d-axis inductance	Shown in Figure 1b
L_q	q-axis inductance	Shown in Figure 1b
R	winding resistance	1.03 Ω
φ_{pm}	rotor flux linkage	0.08483 Wb
E_{coef}	electromotive force coefficient (RMS)	0.02176 V/rpm
J	rotation inertia	3.296×10^{-4} kg·m^2

4.2. Simulation Results

As a means of verifying the effectiveness of the A-DESO, this paper conducted a comparison experiment between the feedback of the A-DESO, the traditional ESO, and without the ESO.

(a) Simulation Set 1: Load and unload experiments in MTPA working conditions.

From the no-load condition to the rated-load condition and opposite operating mode, this group of simulations verified the speed fluctuation. Figure 19 illustrates the change in speed associated with a step load from 0 Nm to 1.9 Nm at t = 3 s and a step load from 1.9 Nm to 0 Nm at t = 6 s. From the simulation, the machine speed experiencess a steady-state error for 74 rpm for a long convergence time while the A-DESO and the ESO experience a 23 rpm steady-state error and the steady-state error is maintained for a considerable period. Meanwhile, the A-DESO shows a better speed dynamic response compared to the ESO part

from (a). The same results can be obtained when a step load occurs from 1.9 Nm to 0 Nm. It can be summarized that the A-DESO has a better speed response performance compared to the ESO and a smaller steady-state error compared to the no-ESO simulation part.

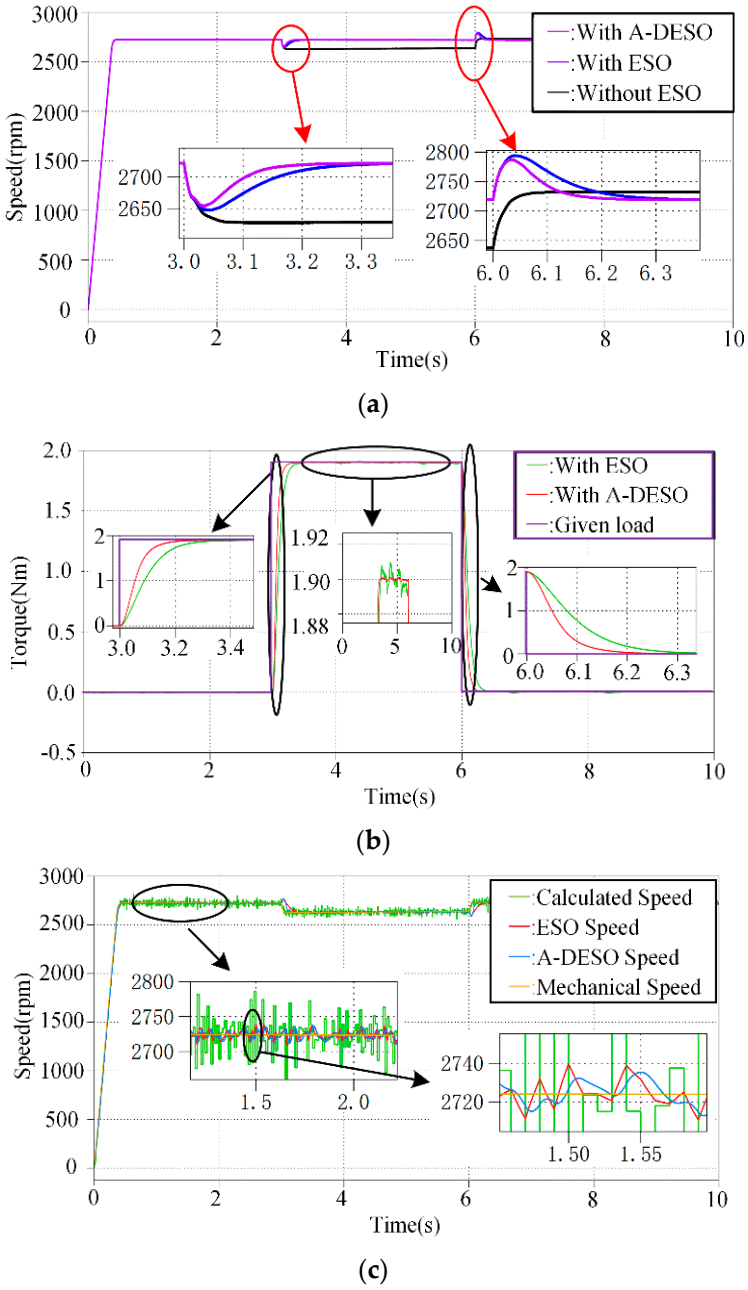

Figure 19. Simulation results on step load response in MTPA region: (**a**) speed fluctuation when load step; (**b**) observed lumped disturbance and given load disturbance; (**c**) comparison of the different speed calculation method.

Figure 19b shows the observed lumped torque disturbance and given load disturbance. It can be obtained that the A-DESO took 0.2 s to stabilize while the ESO took 0.3 s. Meanwhile, the A-DESO featured a small load torque fluctuation compared to the traditional ESO. In Figure 19a,b, it indicates that the A-DESO features a better dynamic performance at low frequencies and better noise immunity at high frequencies. Figure 19c shows that the observed speed from the A-DESO features a smaller speed variation compared to the ESO and the calculated method in the control system.

(b) Simulation Set 2: Load and unload experiments in FW working conditions.

This group of simulations verifies the loading experiments under the working condition of the FW. Figure 20b shows the observed lumped disturbance and given load disturbance when encountering large current noise. It can be found that the A-DESO took 0.05 s to stabilize while the ESO took 0.1 s in the almost same error tolerance.

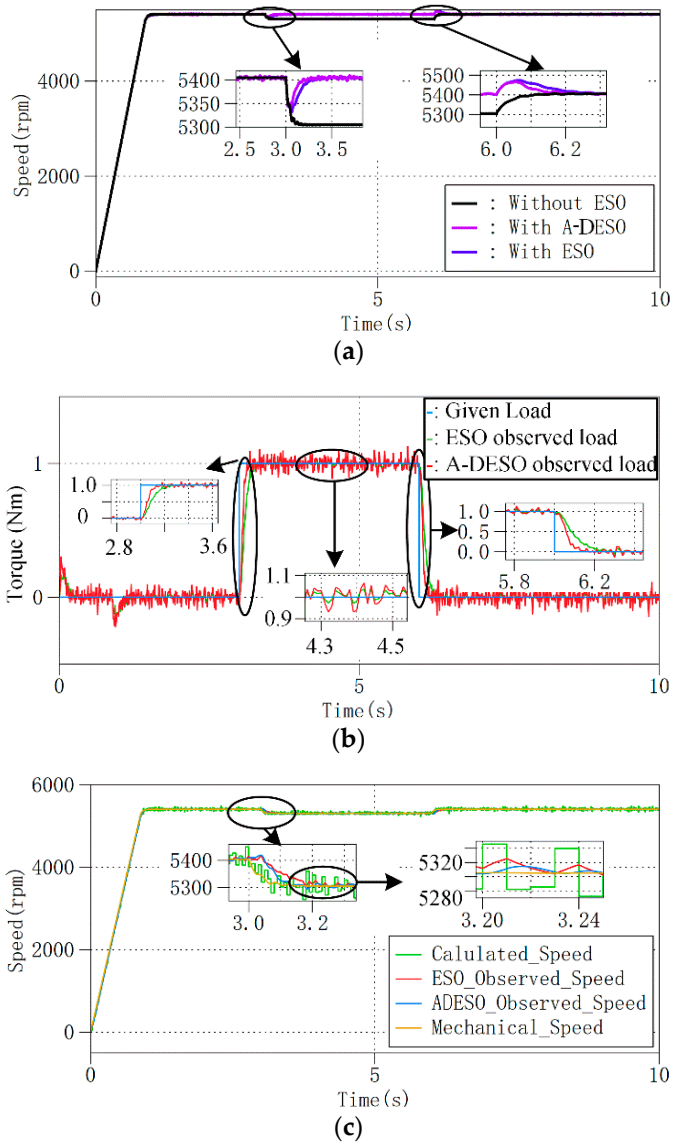

Figure 20. Simulation results on step load response in FW region: (**a**) observed lumped disturbance and given load disturbance; (**b**) speed fluctuation when increasing load under flux weakening control; (**c**) comparison of different speed calculation method in FW condition.

From the no-load condition to the half-load FW condition and opposite operating condition, Figure 20a illustrates the change in speed associated with the step load from 0 Nm to 1.0 Nm at t = 3 s and a step load from 1.0 Nm to 0 Nm at t = 6 s.

From the simulation, the machine speed experiences a steady-state error for 100 rpm for a long convergence time while the A-DESO and the ESO features a 2 rpm steady-state error and the steady-state difference is maintained for a considerable period. Meanwhile, the A-DESO shows a better speed dynamic response compared to the ESO in the same torque error acceptance range. The same results can be obtained when a step load occurs from 1.0 Nm to 0 Nm. It can be summarized that the A-DESO has a better speed response performance compared to the ESO and a small steady-state error compared to the no-ESO

part in the FW working condition. Figure 20c shows that the observed speed from the A-DESO features a smaller speed variation compared to the ESO and the calculated method in the control system. The simulation results could be summarized as Table 2.

Table 2. Simulation Results.

Working Condition		Items		
		PI	**ESO**	**A-DESO**
MTPA 0~1.9 Nm & 1.9~0 Nm	Steady-state Error	74 rpm 31 rpm	23 rpm 20 rpm	23 rpm 20 rpm
	Settle Time	0.6 s 0.35 s	0.3 s 0.3 s	0.2 s 0.2 s
	Noise Content	High	Medium	Low
FW 0–1 Nm & 1–0 Nm	Steady-state Error	100 rpm 2.5 rpm	2 rpm 2 rpm	2 rpm 2 rpm
	Settle Time	0.6 s 0.6 s	0.2 s 0.23 s	0.18 s 0.18 s
	Noise Content	High	Medium	Low

4.3. Experiments Results

(a) Experiment Set 1: In MTPA region

To verify the base speed and FW region, experiments were conducted. According to Figure 21, the step load occurred from 1.5 Nm to 1.9 Nm at 5 s and 1.9 Nm to 1.5 Nm at 25 s.

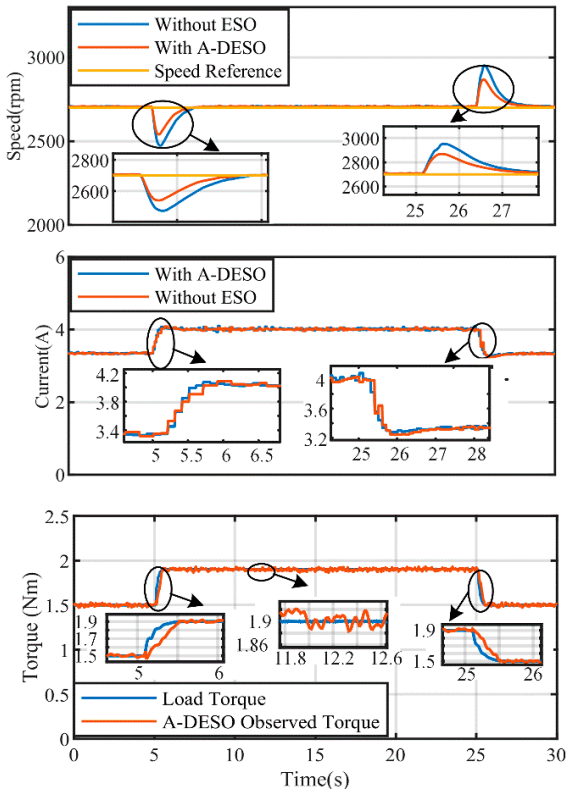

Figure 21. Experiments' results in MTPA region: speed fluctuation with A-DESO and without ESO; current fluctuation with A-DESO and without ESO; load torque and observed disturbance.

As can be seen from the experiment, in the presence of the A-DESO, the maximum speed fluctuation is reduced by 63 rpm and the stabilization time and the current settling time are reduced by 0.2 s. These experiments demonstrate that the A-DESO reduces the speed ripple and shortens the stabilization time at rated speed in the constant speed region.

(b) Experiment Set 2: In FW region

It was found that the A-DESO effects the FW working condition in this group of experiments. Figure 22 shows the torque disturbance, which shows that when the step torque increases, the speed fluctuation of the A-DESO control group is 78 rpm smaller than the ESO group, and the current stabilization time is shortened by 2 s compared to the ESO group. When the load step decreases, the speed fluctuation with the A-DESO is 82 rpm smaller than that of the control group without the ESO, and the current stabilization time is shortened by 2 s. It can be seen from this group of experiments that the A-DESO increases the anti-disturbance performance of the system and reduces the speed fluctuation and current adjustment time.

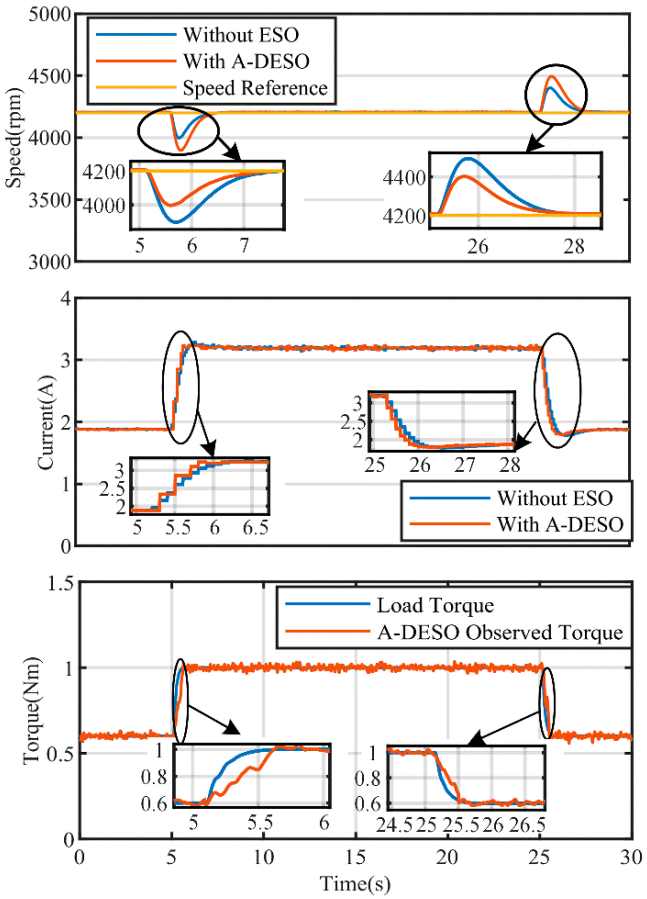

Figure 22. Experiments' results in FW region: speed fluctuation with A-DESO and without ESO; current fluctuation with A-DESO and without ESO; load torque and observed disturbance.

(c) Experiment Set 3: Periodic step load response in MTPA

A set of experiments has been conducted to verify the change in the load cycle. In the below of Figure 23, the load cycle change is shown under the base speed condition, and in the top of Figure 23 the speed fluctuation under the load response is shown. In the experiments, the period of step loads is 3 s as described in the top of Figure 23.

The A-DESO has a better control effect when faced with periodic step loads, as shown by this group of experiments. During the load change cycle, the speed of the control group with the A-DESO stabilized rapidly, whereas the speed of the control group without the ESO failed to stabilize.

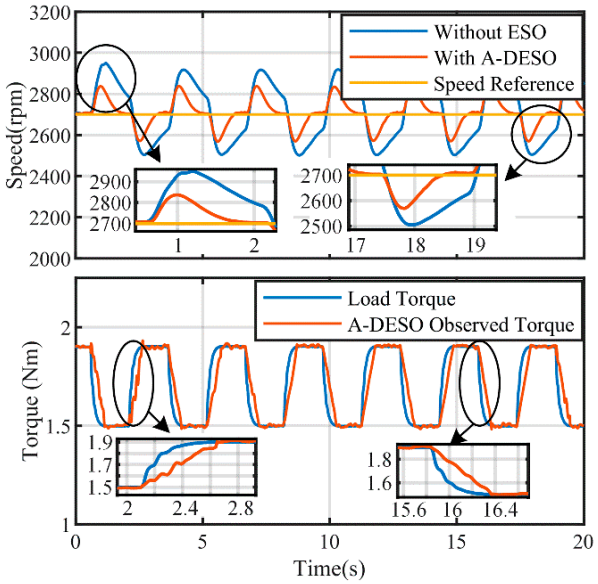

Figure 23. Experiments' results in repeating step-load response in MTPA working condition: speed fluctuation with A-DESO and without ESO; load torque and observed disturbance.

(d) Experiment Set 4: Periodic step load response in FW

A set of experiments has been conducted to verify the change in the load cycle in the FW working condition. In the below of Figure 24, the cycle step load change is shown under the FW condition, and in the top of Figure 24 the speed fluctuation under the load response is shown. In the experiments, the period of step loads is 3 s as described in the below of below of Figure 24.

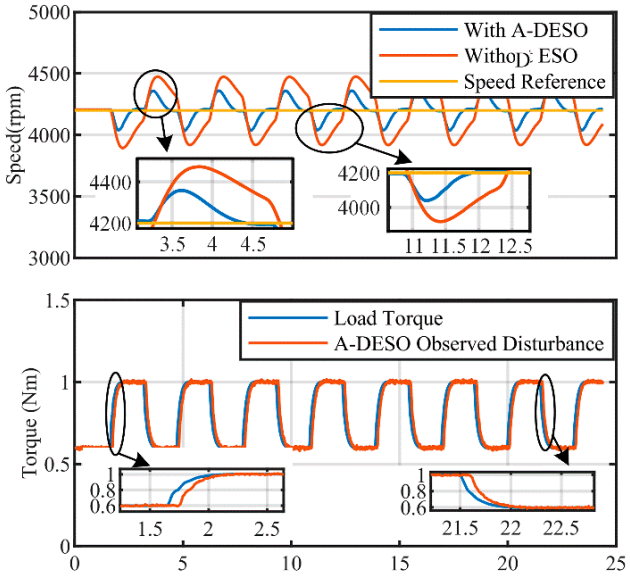

Figure 24. Experiments' results in repeating step-load response in FW working condition: speed fluctuation with A-DESO and without ESO; load torque and observed disturbance.

The same results can be obtained from the previous experiments. The A-DESO has a better control effect when faced with periodic step loads in the FW working condition, as shown by this group of experiments. During the cycle load change, the speed of the control group with the A-DESO stabilized rapidly, whereas the speed of the control group without the ESO failed to stabilize.

(e) Experiment Set 5: Ramp load

A set of experiments has been conducted to verify the change in the ramp load. Figure 24 shows the effect of ramp load tracking in the flux weakening region.

In Figure 25, tracking a ramp load without the ESO resulted in an average static difference in speed of 56 rpm, while tracking a ramp load with the A-DESO resulted in an average static difference of 36 rpm. Studies have shown that the A-DESO can improve the tracking performance of the ramp load and reduce the static error in the tracking state effectively.

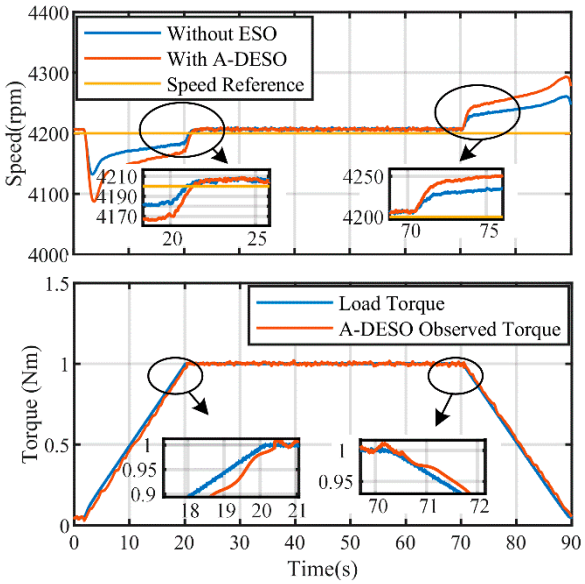

Figure 25. Experiments' results in ramp load response in the whole working condition: speed fluctuation with ESO and without ESO; load torque and observed disturbance.

5. Conclusions

In this paper, a new MTPA and FW control strategy based on an A-DESO and a LUT is proposed, which features a small steady-state error, quick response, and high anti-load disturbance, as well as a current and position signal noise suppression ability. Compared with the traditional ESO, the proposed A-DESO features a lower low-frequency observation error and higher high-frequency noise suppression ability under the same cut-off frequency, which ensures a better stability under the MTPA and FW region and it can reduce the possibility of a rebounding problem between the two working conditions. Strict stability proofs are derived for the proposed A-DESO and error analysis for the proposed A-DESO was carried out considering parameters mismatch. Then, the calculation method of parameters was given based on the PMa-SynRM. The proposed control features an average of 63 rpm overshoot reduction and 0.2 s convergence reduction for the MTPA region. For other working conditions, the same performance improvement can be obtained.

From the simulation and experiments' results, the proposed A-DESO improves the dynamic response of the system in the MTPA region and FW region. Under different load experiments, including step load, periodic step load, and ramp load, the proposed A-DESO features a better ability to reduce the speed fluctuations and response time. Meanwhile, it can effectively suppress the noise caused by a sensor.

Author Contributions: Methodology, Y.B. and X.Z.; Writing—original draft, D.L.; Supervision, S.W., C.G. (Chunyang Gu), C.G. (Chris Gerada) and H.Z. All authors have read and agreed to the published version of the manuscript.

Funding: This work was supported in part by the Ningbo Science and Technology Bureau under Grant 2022Z042 and Grant 2022Z019, and in part by Yongjiang Laboratory. This Project is Supported by Ningbo Natural Science Foundation Programme (Project ID 2023J191).

Data Availability Statement: The original contributions presented in the study are included in the article, further inquiries can be directed to the corresponding author.

Conflicts of Interest: The authors declare no conflict of interest.

References

1. Kong, Y.; Lin, M.; Yin, M.; Hao, L. Rotor Structure on Reducing Demagnetization of Magnet and Torque Ripple in a PMa-synRM With Ferrite Permanent Magnet. *IEEE Trans. Magn.* **2018**, *54*, 8108705. [CrossRef]
2. Jung, D.-H.; Kwak, Y.; Lee, J.; Jin, C.-S. Study on the Optimal Design of PMa-SynRM Loading Ratio for Achievement of Ultrapremium Efficiency. *IEEE Trans. Magn.* **2017**, *53*, 8001904. [CrossRef]
3. Huynh, T.A.; Hsieh, M.-F.; Shih, K.-J.; Kuo, H.-F. An Investigation Into the Effect of PM Arrangements on PMa-SynRM Performance. *IEEE Trans. Ind. Appl.* **2018**, *54*, 5856–5868. [CrossRef]
4. Gao, N.; Li, X.; Wang, F. A Novel Control Method for PMSM in High-Speed Flux Weakening Region Based on PI-Sliding Mode Control. *IEEE Access* **2019**, *7*, 168581–168590.
5. Zhang, Y.; Yin, Z.; Bai, C.; Wang, G.; Liu, J. A Rotor Position and Speed Estimation Method Using an Improved Linear Extended State Observer for IPMSM Sensorless Drives. *IEEE Trans. Power Electron.* **2021**, *36*, 14062–14073. [CrossRef]
6. Shi, T.; Wang, Z.; Xia, C. Speed Measurement Error Suppression for PMSM Control System Using Self-Adaption Kalman Observer. *IEEE Trans. Ind. Electron.* **2015**, *62*, 2753–2763. [CrossRef]
7. Li, H.; Yu, J. Anti-Disturbance Control Based on Cascade ESO and Sliding Mode Control for Gimbal System of Double Gimbal CMG. *IEEE Access* **2020**, *8*, 5644–5654. [CrossRef]
8. Li, D.; Gu, C.; Wang, S.; Zhang, H.; Gerada, C.; Camilleri, R.; Zhang, Y. An Improved Control Strategy of PM-Assisted Synchronous Reluctance Machines Based on an Extended State Observer. In Proceedings of the 2022 IEEE Transportation Electrification Conference and Expo, Asia-Pacific (ITEC Asia-Pacific), Haining, China, 28–31 October 2022; pp. 1–6. [CrossRef]
9. Trancho, E.; Ibarra, E.; Arias, A.; Kortabarria, I.; Jurrgens, J.; Marengo, L.; Fricasse, A.; Gragger, J.V. PM-Assisted Synchronous Reluctance Machine Flux Weakening Control for EV and HEV Applications. *IEEE Trans. Ind. Electron.* **2018**, *65*, 2986–2995. [CrossRef]
10. Wang, T.; Liu, J.; Xu, Z.; Xu, L.; Zhu, Y. Research on sliding mode control of synchronous reluctance motor considering the effect of stator resistance. *IEEE Trans. Ind. Electron.* **2020**, *67*, 70–79.
11. STalole, E.; Kolhe, J.P.; Phadke, S.B. Extended-State-Observer-Based Control of Flexible-Joint System With Experimental Validation. *IEEE Trans. Ind. Electron.* **2010**, *57*, 1411–1419. [CrossRef]
12. Han, J. From PID to Active Disturbance Rejection Control. *IEEE Trans. Ind. Electron.* **2009**, *56*, 900–906. [CrossRef]
13. Han, J. *Active Disturbance Rejection Control Technique-The Technique for Estimating and Compensating the Uncertainties*; National Defense Industry Press: Beijing, China, 2008.
14. Gao, Z. From linear to non-linear control means: A practical progression. *ISA Trans.* **2002**, *41*, 177–189. [CrossRef] [PubMed]
15. Zhao, Z.; Guo, B. A novel extended state observer for output tracking of MIMO systems with mismatched uncertainty. *IEEE Trans. Autom. Control* **2018**, *63*, 211–218. [CrossRef]
16. Zhao, Z.; Guo, B. On active disturbance rejection control for nonlinear systems using time-varying gain. *Eur. J. Control* **2015**, *23*, 62–70. [CrossRef]
17. Attar, M.; Majd, V.J.; Dini, N. Analysis and design of a time-varying extended state observer for a class of non-linear systems with unknown dynamics using spectral Lyapunov function. *J. Intell. Robot. Syst.* **2019**, *94*, 405–421. [CrossRef]
18. Argomedo, F.B.; Krstic, M. Backstepping-forwarding control and observation for hyperbolic PDEs with Fredholm integrals. IEEE Trans. *Autom. Control* **2015**, *60*, 2145–2160. [CrossRef]
19. Zheng, Q.; Gao, L.Q.; Gao, Z. On stability analysis of active disturbance rejection control for non-linear time-varying plants with unknown dynamics. In Proceedings of the 2007 46th IEEE Conference on Decision and Control, New Orleans, LA, USA, 12–14 December 2007; pp. 3501–3506.
20. Yu, J.; Shi, P.; Dong, W.; Chen, B.; Lin, C. Neural network-based adaptive dynamic surface control for permanent magnet synchronous motors. *IEEE Trans. Neural Netw. Learn. Syst.* **2015**, *26*, 640–645. [CrossRef]
21. Liu, W.; Lim, C.; Shi, P.; Xu, S. Backstepping fuzzy adaptive control for a class of quantized non-linear systems. *IEEE Trans. Fuzzy Syst.* **2017**, *25*, 1090–1101. [CrossRef]
22. Sun, L.; Zheng, Z. Disturbance-observer-based robust backstepping attitude stabilization of spacecraft under input saturation and measurement uncertainty. *IEEE Trans. Ind. Electron.* **2017**, *64*, 7994–8002. [CrossRef]
23. Darbha, S.; Hedrick, J.; Yip, P.; Gerdes, J. Dynamic surface control for a class of non-linear systems. *IEEE Trans. Autom. Control* **2000**, *45*, 1893–1899.
24. Niu, B.; Liu, Y.; Zong, G.; Han, Z.; Fu, J. Command filter-based adaptive neural tracking controller design for uncertain switched nonlinear output-constrained systems. *IEEE Trans. Cybern.* **2017**, *47*, 3160–3171. [CrossRef]
25. Li, T.; Wang, D.; Feng, G.; Tong, S. A DSC approach to robust adaptive NN tracking control for strict-feedback non-linear systems. *IEEE Trans. Syst. Man Cybern. Part B-Cybern.* **2010**, *40*, 915–927.
26. Bechlioulis, C.P.; Rovithakis, G. Adaptive control with guaranteed transient and steady state tracking error bounds for strict feedback systems. *Automatica* **2009**, *45*, 532–538. [CrossRef]

27. Bai, W.; Xue, W.; Huang, Y.; Fang, H. On extended state based kalman filter design for a class of nonlinear time-varying uncertain systems. *Sci. China Inf. Sci.* **2018**, *61*, 042201. [CrossRef]
28. Xue, W.; Bai, W.; Yang, S.; Song, K.; Huang, Y.; Xie, H. ADRCwith adaptive extended state observer and its application to air-fuel ratio control in gasoline engines. *IEEE Trans. Ind. Electron.* **2015**, *62*, 5847–5857. [CrossRef]
29. Amin, M.; Aziz, G.A.A.; Durkin, J.; Mohammed, O.A. A Hardware-in-the-Loop Realization of Speed Sensorless Control of PMa-SynRM With Steady-State and Transient Performances Enhancement. *IEEE Trans. Ind. Appl.* **2019**, *55*, 5331–5342. [CrossRef]
30. Du, Y.; Cao, W.; She, J. Analysis and Design of Active Disturbance Rejection Control With an Improved Extended State Observer for Systems With Measurement Noise. *IEEE Trans. Ind. Electron.* **2023**, *70*, 855–865. [CrossRef]